Critical Role of Vertical Radiative Cooling Contrast in Triggering Episodic Deluges in Small-Domain Hothouse Climates

Xinyi Song[1] [ID] **, Dorian S. Abbot[2]** [ID] **, and Jun Yang[1]** [ID]

[1]Laboratory for Climate and Ocean-Atmosphere Studies, Department of Atmospheric and Oceanic Sciences, School of Physics, Peking University, Beijing, China, [2]Department of the Geophysical Sciences, The University of Chicago, Chicago, IL, USA

Abstract Seeley and Wordsworth (2021, https://doi.org/10.1038/s41586-021-03919-z) showed that in small-domain cloud-resolving simulations the temporal pattern of precipitation transforms in extremely hot climates ($\geq$320 K) from quasi-steady to organized episodic deluges, with outbursts of heavy rain alternating with several dry days. They proposed a mechanism for this transition involving increased water vapor greenhouse effect and solar radiation absorption leading to net lower-tropospheric radiative heating. This heating inhibits lower-tropospheric convection and decouples the boundary layer from the upper troposphere during the dry phase, allowing lower-tropospheric moist static energy to build until it discharges, resulting in a deluge. We perform cloud-resolving simulations in polar night and show that the same transition occurs, implying that some revision of their mechanism is necessary. We perform further tests to show that episodic deluges can occur even if the lower-tropospheric radiative heating rate is negative, as long as the magnitude of the upper-tropospheric radiative cooling is about twice as large. We find that in the episodic deluge regime the period can be predicted from the time for radiation and reevaporation to cool the lower atmosphere.

Plain Language Summary Precipitation plays an important role in Earth's climate and habitability, and also influences important weathering processes such as the carbonate-silicate cycle. In the distant future, Earth may experience a very hot and wet "hothouse" climate, just like it may have in the Archean. Modeling results show that in a hothouse climate, precipitation transforms into an "episodic deluge" pattern, with outbursts of heavy rain alternating with several dry days. In this study, we find that positive lower-tropospheric heating is not the necessary cause for episodic deluges. Instead, vertical radiative cooling contrast is critical in triggering the episodic deluges in small-domain hothouse climates. We also try to understand the underlying mechanism of episodic deluges through CIN and CAPE analyses.

1. Introduction

Earth might have experienced an extremely warm and wet climate, a "hothouse," in the Archean (Charnay et al., 2017; Sleep, 2010; Steffen et al., 2018), or in the aftermath of a snowball Earth event (Higgins & Schrag, 2003; Hir et al., 2009; Hoffman et al., 2017; Pierrehumbert et al., 2011; Yang et al., 2017), and may experience a hothouse climate again in the distant future (Goldblatt et al., 2013; Ingersoll, 1969; Kasting et al., 1984; Kidder & Worsley, 2012; Leconte et al., 2013; Ramirez et al., 2014). Previous work mainly used general circulation models (GCMs), and concluded that there could be a lower-tropospheric temperature inversion and significant increase in upper-tropospheric cloud cover in hothouse climates (Popp et al., 2016; Wolf et al., 2018; Wolf & Toon, 2015; Wordsworth & Pierrehumbert, 2013). Seeley and Wordsworth (2021) advanced the field by using convective-scale cloud-resolving models and found that the precipitation would organize in time into an "episodic deluge" pattern. In this regime, the majority of the grid points have an outburst of heavy rain at the same time (Figure 4d in Seeley and Wordsworth (2021)), followed by several dry days. Seeley and Wordsworth (2021) investigated this in three different cloud-resolving models, Das Atmosphärische Modell (DAM) (Romps, 2008), the System for Atmospheric Modeling (SAM) (M. F. Khairoutdinov & Randall, 2003), and the Cloud Model 1 (CM1) (Bryan & Fritsch, 2002), and modified the radiative transfer scheme of DAM in order to be more accurate in hot climates. They verified that the onset of episodic deluges does not depend on the specific model choice. Most of their experiments are in a small domain of 72 km × 72 km, and the episodic deluge is a synchronized behavior between the grid points.
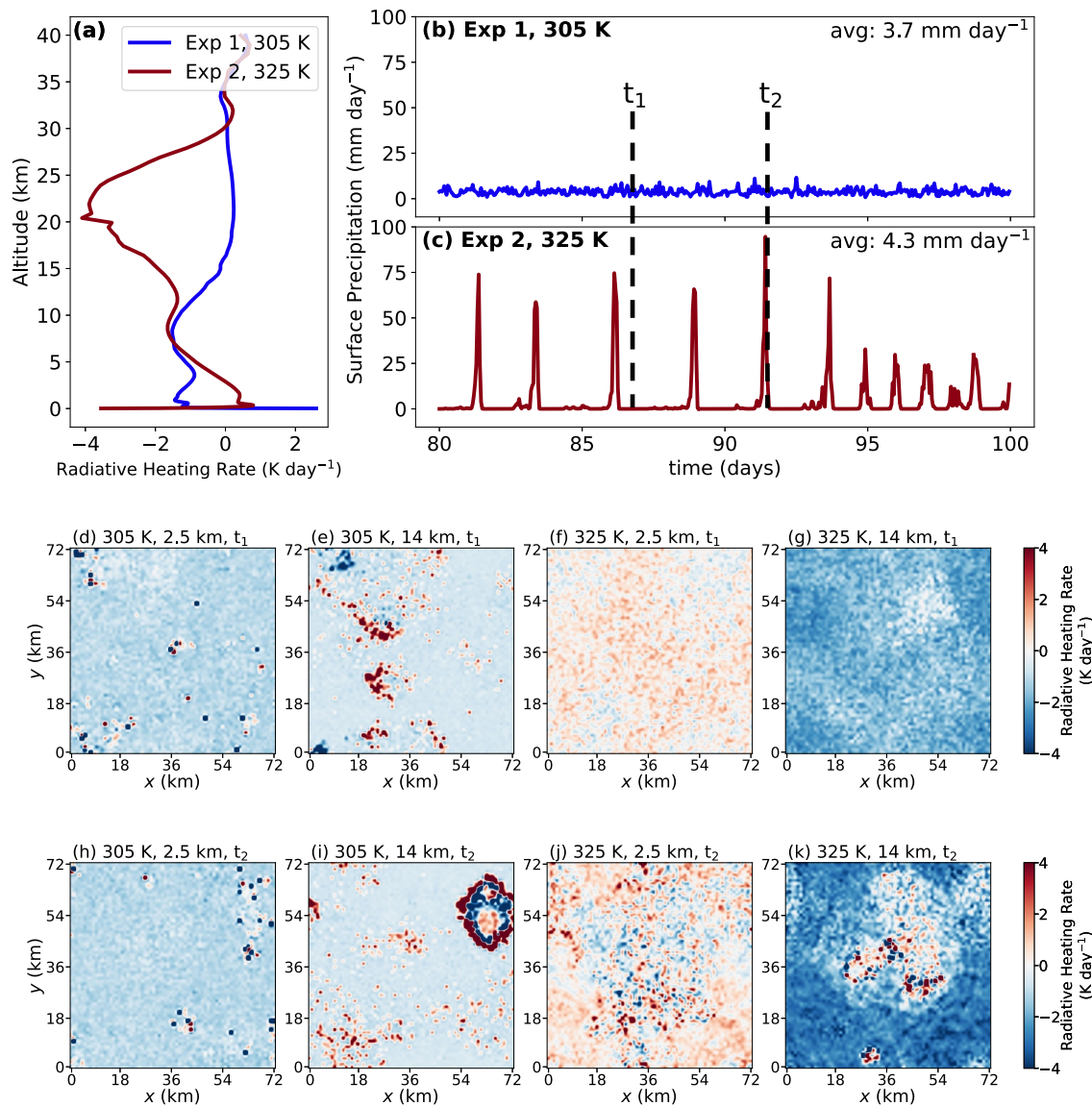
Figure 1. Reproduction of modeling results of Seeley and Wordsworth (2021) using SAM. Panel (a) shows the radiative heating rate averaged over the last 20 days. Panels (b) and (c) show the precipitation pattern in two simulations with the surface temperature fixed at 305 K (Exp 1) and 325 K (Exp 2), respectively. Panels (d)–(g) show the horizontal distribution of the radiative heating rate (longwave plus shortwave) for both cases during a dry spell of Exp2 (t_1). Panels (h)–(k) show the horizontal distributions during a convective period of Exp 2 (t_2). Each case shows slices at 2.5 and 14 km above the surface. For time variations, see the video version in Supporting Information S1. Both cases are run for 100 days. The heating rate near the surface is positive in Exp 1 for reasons we do not currently understand.

Seeley and Wordsworth (2021) argued that episodic deluges are caused by lower-tropospheric radiative heating: When the climate is warm enough, the water vapor greenhouse effect intensifies and eventually closes off infrared spectral windows. The lower atmosphere gets optically thick and longwave cooling rate drops to almost zero (Koll & Cronin, 2018; Seeley & Jeevanjee, 2021; Wolf & Toon, 2015; Wordsworth & Pierrehumbert, 2013). More lower-tropospheric water vapor also increases near-infrared absorption, and results in a net positive heating rate. Atmospheric absorption of solar radiation therefore plays an important role in their mechanism. Figure 1 shows our reproduction of the results of Seeley and Wordsworth (2021) using the cloud-resolving model SAM. When the surface temperature is 305 K (Exp 1), there is net radiative cooling in the lower troposphere (blue line in Figure 1a), and the precipitation pattern is quasi-steady (Figure 1b). When the surface temperature is 325 K (Exp 2), the lower-tropospheric radiative heating rate becomes positive (red line in Figure 1a), and episodic deluges occur.

The heating rate profiles undergo three major changes as the surface temperature increases to 325 K. First, the lower troposphere shifts from cooling to heating. Second, the vertical gradient of the heating rate profile increases (Figure 1a, see also Figure 2b in Seeley and Wordsworth (2021)). When the surface temperature is 305 K, the radiative heating rate is about -1.5 K day^{-1} from the near surface layer to about 10 km, then smoothly transits to 0 K day^{-1} in the stratosphere (blue line in Figure 1a). When the surface temperature is 325 K, the lower-tropospheric radiative heating rate is about 0.5 K day^{-1} at about 2 km, but the upper-tropospheric radiative heating rate is about -4 K day^{-1} at 20 km (the red line in Figure 1a). The radiative heating rate in the upper troposphere is more negative when the surface temperature is higher because the air is warmer and less dense, leading to lower thermal inertia. Third, during the dry period, the horizontal distribution of radiative heating is much more homogenous for the 325 K case, both at the lower troposphere (Figure 1f) and in the upper troposphere (Figure 1g). Note that the heating rates for the 325 K case are fairly heterogeneous horizontally during convection (Figures 1j and 1k). For the video version of Figure 1, see Movie S1.

Seeley and Wordsworth (2021) pointed to lower-tropospheric radiative heating driven primarily by shortwave absorption as the primary factor leading to episodic deluges. In this paper, we suggest instead that the vertical gradient of radiative cooling is a more important factor for the onset of episodic deluges. This point is emphasized by the fact that episodic deluges can occur even during polar night and when the radiative heating rate in the lower troposphere is negative (Section 2). More specifically, episodic deluges require that the magnitude of radiative cooling in the upper-troposphere be about twice that in the lower troposphere (Section 3.4). Finally, we show that in the episodic deluge regime the length of the deluge can be predicted from the time for radiation and reevaporation to cool the lower troposphere (Section 3.5).

2. Episodic Deluges During Polar Night

All the experiments in this study use version 6.11.6 of SAM (M. F. Khairoutdinov & Emanuel, 2018; M. F. Khairoutdinov & Randall, 2003), one of the three models used in Seeley and Wordsworth (2021). The horizontal resolution in each experiment is 2 km with 72 grid points in each direction. The vertical resolution is 144 grid points within 64 km. CO_2 is set to 400 ppmv and the experiments do not contain ozone. The microphysics scheme is SAM's 1-moment scheme, which uses only mass as the prognostic variable. The radiation scheme in the reproduction experiments (Exp 1 and 2) is RRTM (Mlawer et al., 1997), same as the SAM experiments in Seeley and Wordsworth (2021). RRTM uses different lookup tables for water vapor absorption below and above 100 hPa. Under high temperature, when water vapor concentration near 100 hPa is large, RRTM produces discontinuous heating rates (as shown in Extended Data Figure 1 in Seeley & Wordsworth, 2021). For the experiments in Section 2 (Exp 3 and 4), the radiation scheme is CAM (Collins et al., 2006) with an updating frequency of every 90 time steps, and each time step is 10 s. Although both RRTM and CAM are not accurate enough under high temperature (Collins et al., 2006; Yang et al., 2016), both are able to simulate episodic deluges (Dagan et al., 2023; Seeley & Wordsworth, 2021). The 2D time-height output statistics are hourly averages, and 3D output statistics are hourly snapshots.

The initial conditions of our experiments are climate states that are close to the balanced results. For example, the initial condition for Exp 4 is the average climate state for the last 20 days of Exp 3. The initial condition for the experiments in Section 3 below is the average climate state for the last 20 days of Exp 2. Through experiment tests, we have found that the results are not sensitive to the initial conditions.

We find episodic deluges in polar night simulations, demonstrating that shortwave heating is not necessary for episodic deluges (Figure 2). These polar night simulations only include longwave radiation transfer. The experiments do not include shortwave incident, seasonal cycle, or diurnal cycle. We find polar night episodic deluges both with a fixed sea surface temperature of 330 K (Exp 3) and with a two-m-deep slab ocean and a positive ocean heat flux of 230 W m^{-2} (Exp 4). Exp 4 has a similar sea surface temperature to that of Exp 3. In both cases there are deluges with a peak precipitation of about 80 mm day^{-1} that lasts several hours. These deluges are intense and are comparable with WMO's standard for heavy rain: "rainfall greater than or equal to 50 mm in the past 24 hr (https://severeweather.wmo.int/raindoc.html)." In this paper, a deluge is a convective period in which peak precipitation reaches about several to 10 times the average rate. Deluges are followed by dry, inhibition periods that last several days during which the precipitation rates are usually below 2 mm day^{-1}.

So far, the polar night simulations indicate that shortwave heating is not a necessary condition for episodic deluges, but we still cannot rule out the necessity of lower-tropospheric radiative heating, as the heating rate at
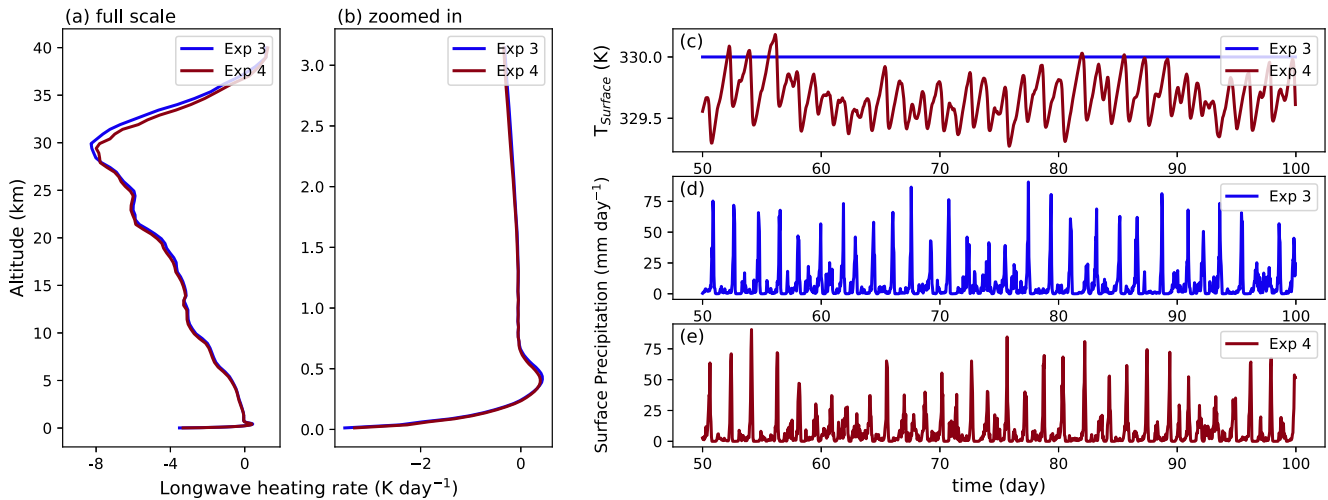
Figure 2. Full scale (a) and zoomed in (b) radiative heating rate profiles in polar night hothouse climate. Both profiles are averaged over the last 50 days. One experiment fixes the sea surface temperature (SST) at 330 K (Exp 3). The other includes an ocean heat import of 230 W m^{-2} (Exp 4), in order to maintain the SST at around 330 K (c). Episodic deluges occur in both experiments (d and e).

about 0.5 km is slightly positive (Figures 2a and 2b). We find a 0.2–0.3 K temperature inversion between the surface and the lowest layer of the atmosphere for Exp 3 and Exp 4 (figure not shown). The temperature inversion could be the cause of this positive heating rate, but future studies would be required to confirm this.

To exclude the influence of this positive longwave heating, we add an additional experiment, Exp 5, to smooth the near surface layer of the heating rate profile in the polar night experiment, and set the maximum value to 0 K day^{-1}, as shown in Figure 3a. Episodic deluges still occur under this radiative heating profile (Figure 3b). Therefore, we can confirm that lower-tropospheric radiative heating is not necessary for episodic deluges. Seeley and Wordsworth were also aware of the fact that lower-tropospheric radiative heating is unnecessary, but they did not include it in Seeley and Wordsworth (2021) due to the length constraints of the Nature journal (Jacob Seeley, personal communication, 7 November 2023).

What is necessary to cause episodic deluges? Let's take a look back at Figure 1a. Another important feature that changes between the 305 and 325 K cases is the vertical gradient in the heating rate: the upper-tropospheric cooling is much stronger in the 325 K case, leading to a larger vertical gradient. In the following sections, we use modeling experiments to investigate how different heating rate profiles can influence the episodic deluges.

3. Heating Rate Profile Experiments and Results

The following experiments are run for 100 days with a fixed sea surface temperature of 325 K. All experiments restart from the 325 K simulation Exp 2. The radiative heating rate profile in Exp 2 (red line in Figure 1a) can be roughly divided into three distinct regions: a lower troposphere, an upper troposphere with strong cooling, and a stratosphere with a radiative heating near zero. Given this qualitative pattern, we prescribe radiative heating rate profiles in a three-layer structure as shown in Figure 4. The heating rate profiles do not evolve with time, so both longwave and shortwave radiative transfer are turned off in the model. The transitions between layers are smooth, so we use hyperbolic functions to describe the heating rate profiles. The heating rate profiles are given by,

$$\gamma = \begin{cases} A_{tro} \dfrac{a^{-z^*} - a^{z^*}}{a^{-z^*} + a^{z^*}} + B_{tro}, & \text{for the troposphere,} \\[3mm] A_{stra} \dfrac{a^{-z^*} - a^{z^*}}{a^{-z^*} + a^{z^*}} + B_{stra}, & \text{for the stratosphere,} \end{cases} \tag{1}$$

where γ is the radiative heating rate in units of K day^{-1}, z^* is a relative height explained below, a is a dimensionless number that controls the smoothness of the profiles, and here $a = 1.5$. Coefficients γ_0, γ_1, and z_0 control
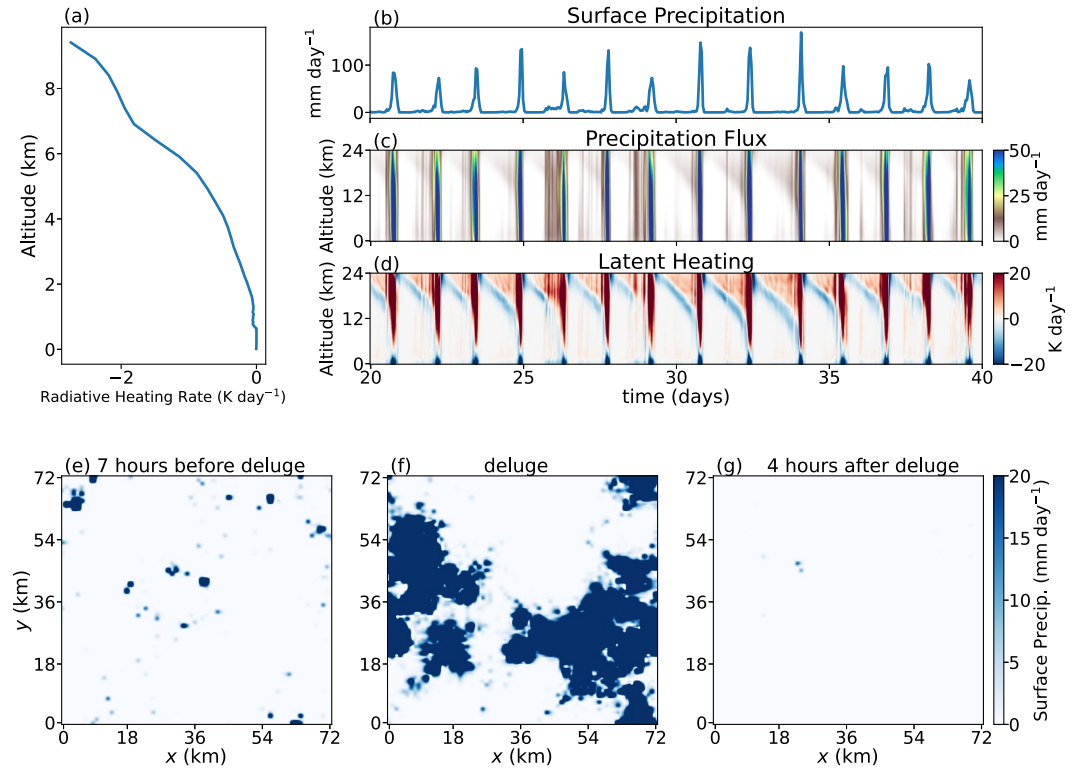
Figure 3. Exp 5: Prescribed radiative heating rate with lower-tropospheric radiative heating removed (a) and simulated precipitation (b) during polar night. Panels (c) and (d) show the altitude-time plot of precipitation flux and latent heating. Panels (e)–(g) show snapshots of surface precipitation at 7 hr before a deluge, during the deluge, and 4 hr after the deluge, respectively. Episodic deluges still exist even if there is no lower-tropospheric radiative heating.

the width and the central point of the heating rate profile, as shown in Figure 4. In the troposphere, $z* = z - z_0$, $A_{tro} = \gamma_0 - \gamma_1$, and $B_{tro} = \frac{\gamma_0 + \gamma_1}{2}$. In the stratosphere, $z* = z - 35$, $A_{stra} = \gamma_1$, and $B_{stra} = \frac{0 + \gamma_1}{2}$.

In the following sections we conduct 4 groups of experiments (Table 1) focusing on three factors: experiments in group one (G1) focus on the influence of the lower-tropospheric radiative heating rate, γ_0; experiments in G2 and G3 focus on the influence of the upper-tropospheric radiative heating rate, γ_1; experiments in G4 focus on the height of the lower troposphere, z_0.

3.1. The Effect of Lower-Tropospheric Heating Rate (γ_0)

First, we check the influence of the lower-tropospheric radiative heating rate while controlling other factors. Figure 5a shows the radiative heating rate profiles in the first group of experiments (G1). The stratospheric heating rate is 0 K day^{-1} and the upper-tropospheric heating rate γ_1 is −1.5 K day^{-1}. The top of the lower troposphere z_0 is 8 km. The lower-tropospheric heating rates γ_0 are 0.2, 0, −0.2, −0.5, −0.8, and −1.2 K day^{-1}, respectively.

To quantify the presence of episodic deluges we define a metric $\alpha \equiv \frac{N_{below}}{N}$ where N_{below} measures the number of days with precipitation below a third of the average value and N measures the total days. The larger α is, the longer the inhibition period is, which means precipitation is concentrated in short deluges. Table 1 shows the result. The value of α can only roughly measure episodic deluges. For most simulations with episodic deluges, $\alpha > 0.5$, but for simulations with α close to 0.5, the situation is uncertain. Some involve episodic deluges (such as G4-2), and some are intermediate between quasi-steady and episodic deluge (such as G2-1). For reference, we use Gini coefficient (Gini, 1997) as another measurement of episodic deluges. The Gini coefficient (G) is given by,

$$G = \frac{\sum_{i=1}^{n} \sum_{j=1}^{n} |x_i - x_j|}{2n^2 \bar{x}}. \tag{2}$$
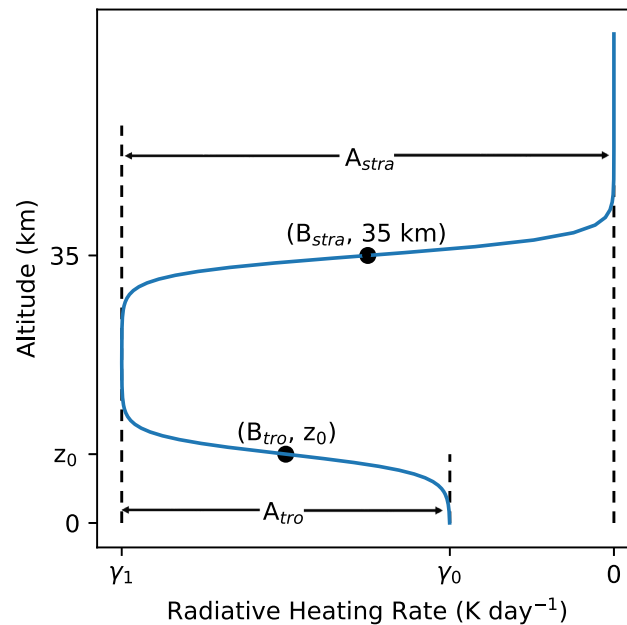
Figure 4. Illustration of the prescribed radiative heating rate profile. The profile can be divided into three parts. The lower troposphere spans from the surface to z_0, with a highest radiative heating rate of γ_0. The upper troposphere, with the most negative radiative heating rate of γ_1, spans from z_0 to 35 km. The stratosphere spans from 35 km to the model top with a highest radiative heating rate of 0 K day^{-1}. The layers are connected to each other smoothly.

G is a measure of statistical dispersion in a group. The lager the Gini coefficient is, the higher precipitation dispersion is. Because the precipitation time series is too short, both metrics, α and G, cannot match episodic deluges perfectly. Undetermined intermediate state always exist around $\alpha = 0.5$ and $G = 0.65$ criteria threshold.

Figures 5b–5g show the surface precipitation. Episodic deluges happen even if the lower-tropospheric radiative heating rate is -0.2 K day^{-1} (Figure 5d), so again positive lower-tropospheric radiative heating is not required for episodic deluges. When the lower-tropospheric radiative heating rate is greater than -0.2 K day^{-1}, precipitation is strongly concentrated in the deluges (Figures 5b–5d). Precipitation during the inhibition period is close to zero and the convective period is short, so $\alpha > 0.5$. As the lower-tropospheric radiative heating rate slowly moves toward a negative value the randomness of precipitation gradually increases into a quasi-steady pattern, so α decreases. When the lower-tropospheric radiative heating rate is less than -0.5 K day^{-1}, the precipitation pattern is no longer episodic but completely random (Figures 5f and 5g). Although the lower-tropospheric heating rate is unlikely in a hothouse climate with solar heating, our experiments have theoretical value.

We also carry out another set of experiments with heating rate profiles that are discontinuous at z_0 and at 35 km to exclude the influence of the transition details between the lower and upper troposphere. The heating rate profile settings are the same as those in G1, but the transitions are sharp (Figure A1a). The results are similar (Figure A1). The less-negative the lower-tropospheric radiative heating rate is, the more episodic the precipitation pattern is. Episodic deluges can occur even with a negative lower-tropospheric heating rate of -0.2 K day^{-1}.

3.2. The Effect of Upper-Tropospheric Heating Rate (γ_1)

Under what conditions will the negative lower-tropospheric radiative heating trigger episodic deluges? We examine the effect of upper-tropospheric heating rate while keeping the lower-tropospheric heating rate negative in the second group of experiments (G2). Figure 6a shows the radiative heating rate profiles. The stratospheric heating rate is 0 K day^{-1} and the lower-tropospheric heating rate, γ_0, is -0.2 K day^{-1}. The top of the lower troposphere z_0 is 8 km. The upper-tropospheric heating rates, γ_1, are -0.2, -0.3, -0.5, -0.7, -1.0, and -1.5 K day^{-1}, respectively.

Figures 6b–6g show the surface precipitation. When the lower-tropospheric heating rate is negative, the upper-tropospheric cooling rate needs to be large enough to trigger episodic deluges. In this set of experiments,

Table 1
Summary of the Results Including Convective Inhibition (CIN) and Convective Available Potential Energy (CAPE) for All the Experiments

Group	Configuration[a]	CIN $(-2\sigma, +2\sigma)$ J kg^{-1}	CAPE $(+2\sigma, -2\sigma)$ J kg^{-1}	α	G	Precipitation
Exp 1	SST = 305 K	0 (0, 0)	6419 (6687, 0)	0.03	0.25	quasi-steady
Exp 2	SST = 325 K	−40 (−97, −19)	2991 (3819, 2054)	0.70	0.85	*episodic*
Exp 3	polar night, SST = 330 K	−55 (−114, −34)	1687 (2283, 910)	0.54	0.73	*episodic*
Exp 4	polar night, slab ocean SST ≈ 330 K	−56 (−118, −35)	1647 (2179, 886)	0.51	0.70	*episodic*
Exp 5	polar night, fixed heating rate, SST = 330 K	−61 (−143, −35)	1649 (2589, 742)	0.66	0.81	*episodic*
G1-1	$\gamma_0 = 0.2, \gamma_1 = -1.5, z_0 = 8$	−56 (−177, −11)	3443 (4926, 1672)	0.93	0.98	*episodic*
G1-2	$\gamma_0 = 0, \gamma_1 = -1.5, z_0 = 8$	−28 (−115, −11)	3019 (4409, 1414)	0.86	0.94	*episodic*
G1-3	$\gamma_0 = -0.2, \gamma_1 = -1.5, z_0 = 8$	−24 (−87, −12)	2980 (3823, 1890)	0.69	0.84	*episodic*
G1-4	$\gamma_0 = -0.5, \gamma_1 = -1.5, z_0 = 8$	−19 (−38, −11)	2899 (3257, 2392)	0.37	0.57	undetermined
G1-5	$\gamma_0 = -0.8, \gamma_1 = -1.5, z_0 = 8$	−16 (−25, −11)	2780 (2970, 2556)	0.17	0.42	quasi-steady
G1-6	$\gamma_0 = -1.2, \gamma_1 = -1.5, z_0 = 8$	−16 (−25, −11)	2745 (2921, 2537)	0.18	0.40	quasi-steady
G2-1	$\gamma_0 = -0.2, \gamma_1 = -0.2, z_0 = 8$	−8 (−18, −4)	2811 (3015, 2507)	0.48	0.65	undetermined
G2-2	$\gamma_0 = -0.2, \gamma_1 = -0.3, z_0 = 8$	−15 (−39, −9)	3213 (3593, 2549)	0.55	0.73	undetermined
G2-3	$\gamma_0 = -0.2, \gamma_1 = -0.5, z_0 = 8$	−16 (−63, −9)	3033 (3603, 2151)	0.64	0.80	*episodic*
G2-4	$\gamma_0 = -0.2, \gamma_1 = -0.7, z_0 = 8$	−17 (−54, −10)	3025 (3548, 2289)	0.60	0.78	*episodic*
G2-5	$\gamma_0 = -0.2, \gamma_1 = -1.0, z_0 = 8$	−21 (−78, −11)	2856 (3624, 1797)	0.68	0.83	*episodic*
G2-6	$\gamma_0 = -0.2, \gamma_1 = -1.5, z_0 = 8$	−23 (−78, −11)	2940 (3756, 1912)	0.69	0.84	*episodic*
G3-1	$\gamma_0 = \gamma_1 = -1$	−17 (−41, −12)	2750 (2916, 2554)	0.15	0.39	quasi-steady
G3-2	$\gamma_0 = \gamma_1 = -2$	−14 (−34, −10)	2661 (2826, 2523)	0.07	0.30	quasi-steady
G3-3	$\gamma_0 = \gamma_1 = -3$	−12 (−39, −8)	2634 (2829, 2380)	0.04	0.24	quasi-steady
G3-4	$\gamma_0 = \gamma_1 = -4$	−10 (−35, −7)	2703 (3033, 2397)	0.01	0.21	quasi-steady
G3-5	$\gamma_0 = \gamma_1 = -5$	−9 (−34, −6)	2746 (3142, 2324)	0.01	0.20	quasi-steady
G4-1	$\gamma_0 = 0, \gamma_1 = -5, z_0 = 3$	−26 (−56, −12)	2768 (3210, 2138)	0.20	0.46	quasi-steady
G4-2	$\gamma_0 = 0, \gamma_1 = -5, z_0 = 5$	−33 (−73, −14)	2797 (3489, 2025)	0.48	0.68	*episodic*
G4-3	$\gamma_0 = 0, \gamma_1 = -5, z_0 = 7$	−41 (−118, −15)	2913 (4060, 1579)	0.70	0.86	*episodic*
G4-4	$\gamma_0 = 0, \gamma_1 = -5, z_0 = 9$	−36 (−126, −11)	3079 (4250, 1598)	0.81	0.91	*episodic*
G4-5	$\gamma_0 = 0, \gamma_1 = -5, z_0 = 11$	−35 (−122, −13)	3269 (4348, 1836)	0.85	0.91	*episodic*
G4-6	$\gamma_0 = 0, \gamma_1 = -5, z_0 = 13$	−30 (−111, −13)	3411 (4358, 2024)	0.87	0.92	*episodic*

[a]γ_0: the lower-tropospheric radiative heating rate in units of K day^{-1}. γ_1: the upper-tropospheric radiative heating rate in units of K day^{-1}. z_0: the height of the lower troposphere in units of km.

episodic deluges exist when the upper-tropospheric heating rate is less than −0.5 day^{-1} (Figures 6d–6g). The stronger the upper-tropospheric cooling is, the shorter the cycle period is, the more concentrated the precipitation is in the deluges, and the larger α is.

We also carry out a set of similar experiments with discontinuous heating rate profiles. The radiative heating rates for the lower troposphere, upper troposphere, and stratosphere are exactly the same as in G2, only the transitions between layers are sharp. The results are similar (Figure A2) except for the exact period of episodic deluges. In general, periods with discontinuous heating rate profiles are longer than periods with smoothed profiles.

Figure 6 suggests that the upper-tropospheric radiative cooling needs to be strong in order to trigger episodic deluges. What if the lower-tropospheric and upper-tropospheric radiative cooling are both strong? Our third group of experiments (G3) set the lower troposphere and upper troposphere to have the same heating rate, that is, $\gamma_0 = \gamma_1$. The stratospheric heating rate is 0 K day^{-1}. The lower-tropospheric and upper-tropospheric heating rates are −1, −2, −3, −4, and −5 K day^{-1}, respectively. The heating rate profiles are similar to those in Figure 2a in Seeley and Wordsworth (2021), but they focused on changing the troposphere height and we focus on changing the
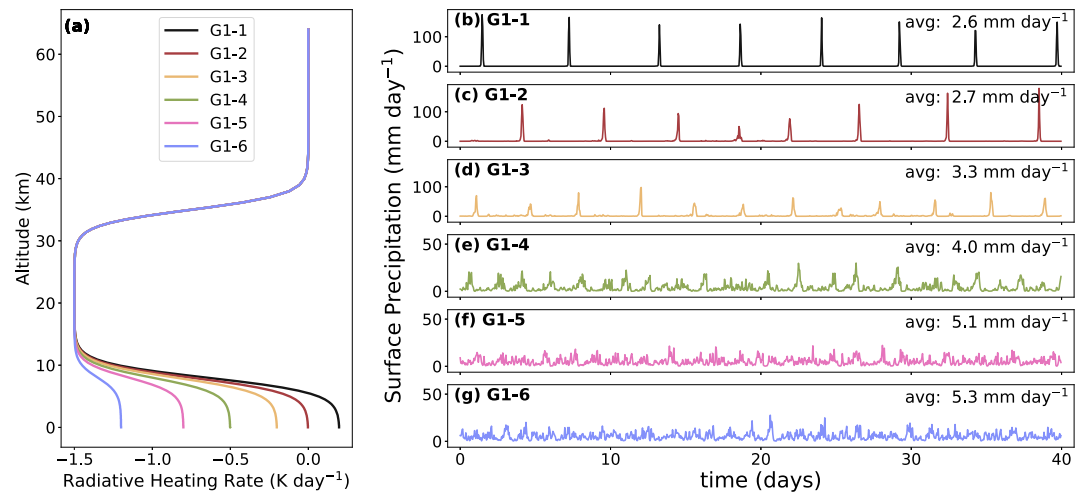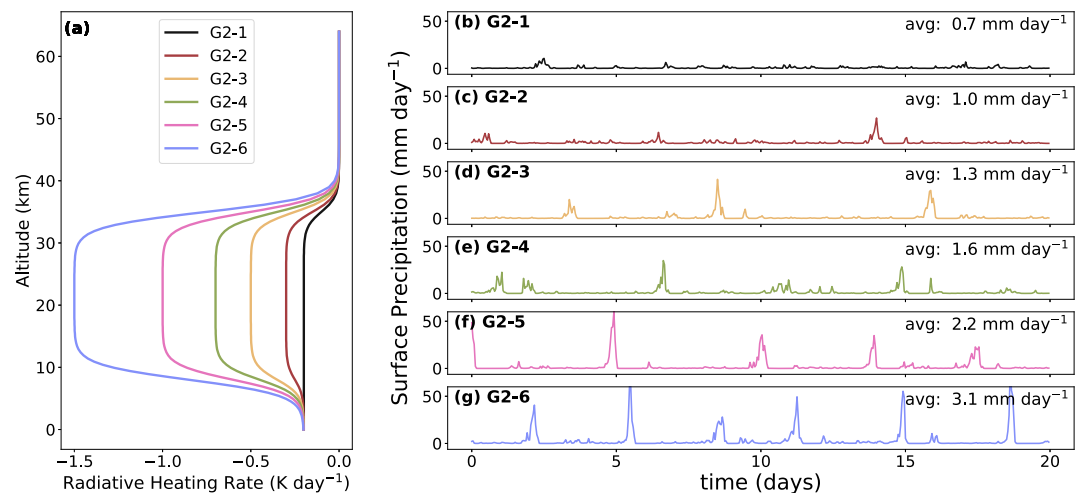
Figure 5. Simulations with fixed upper-tropospheric heating rate and different lower-tropospheric heating rates. Panel (a) shows the prescribed radiative heating rate profiles. The upper-tropospheric heating rate is -1.5 K day^{-1}. The lower-tropospheric heating rates in panels (b) to (g) are 0.2, 0, -0.2, -0.5, -0.8, and -1.2 K day^{-1}, respectively. The top of the lower troposphere is 8 km.

tropospheric heating rate. Figure 7 shows the results. Precipitation patterns in G3 are all quasi-steady, showing that uniform strong radiative cooling is not enough to trigger episodic deluges. This highlights the fact that the vertical gradient in radiative cooling is more important for episodic deluges than the magnitude of radiative cooling. We also carry out a set of similar experiments with discontinuous heating rate profiles. The precipitation patterns are also quasi-steady (Figure A3).

3.3. The Effect of the Top of the Lower Troposphere (z_0)

The top of the lower troposphere (z_0) is the last factor we test. Figure 8a shows the radiative heating rate profiles in the fourth group of experiments (G4). Both the stratospheric and lower-tropospheric heating rates γ_0 are 0 K day^{-1}. The upper-tropospheric heating rate γ_1 is -5 K day^{-1}. The top of the lower troposphere z_0 is 3, 5, 7, 9, 11, and 13 km, respectively.

Figure 6. Simulations with fixed lower-tropospheric heating rate and different upper-tropospheric cooling rates. Panel (a) shows the prescribed radiative heating rate profiles. The lower-tropospheric heating rate is -0.2 K day^{-1}. The upper-tropospheric heating rates in panels (b) to (g) are -0.2, -0.3, -0.5, -0.7, -1.0, and -1.5 K day^{-1}, respectively. The top of the lower troposphere is 8 km.
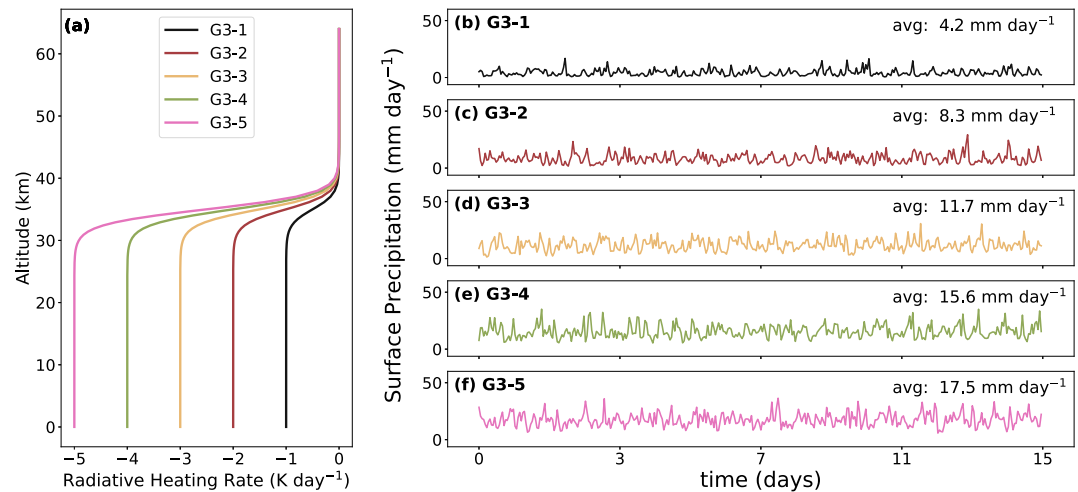
Figure 7. Simulations when lower-tropospheric heating rates and upper-tropospheric cooling rates are the same. Panel (a) shows the prescribed radiative heating rate profiles. The lower-tropospheric heating rates and the upper-tropospheric heating rates in panels (b) to (f) are -1, -2, -3, -4, and -5 K day^{-1}, respectively.

Most of the cases have episodic deluges, but if the lower troposphere is not high enough, 3 km for example, the precipitation pattern is quasi-steady and $\alpha < 0.5$ (Figure 8b). As z_0 increases from 5 to 13 km, the period increases from ≈ 1 to ≈ 3 days. We will discuss the factors determining the period in Section 3.5.

We also carry out a set of experiments with discontinuous heating rate profiles (Figure A4) and the results are almost the same. The discontinuous heating rate profiles, compared with smoothed profiles, have somewhat higher z_0 (Figure A4a vs. Figure 8a). Because of higher z_0, precipitation patterns with discontinuous heating rates (Figures A4b & A4c) are more episodic than the precipitation patterns with smoothed heating rates (Figures 8b and 8c).

3.4. What Is the Underlying Mechanism?

The results of the experiments above with prescribed heating rates can be divided into three types: episodic deluges with positive lower-tropospheric heating rate, episodic deluges with negative lower-tropospheric heating
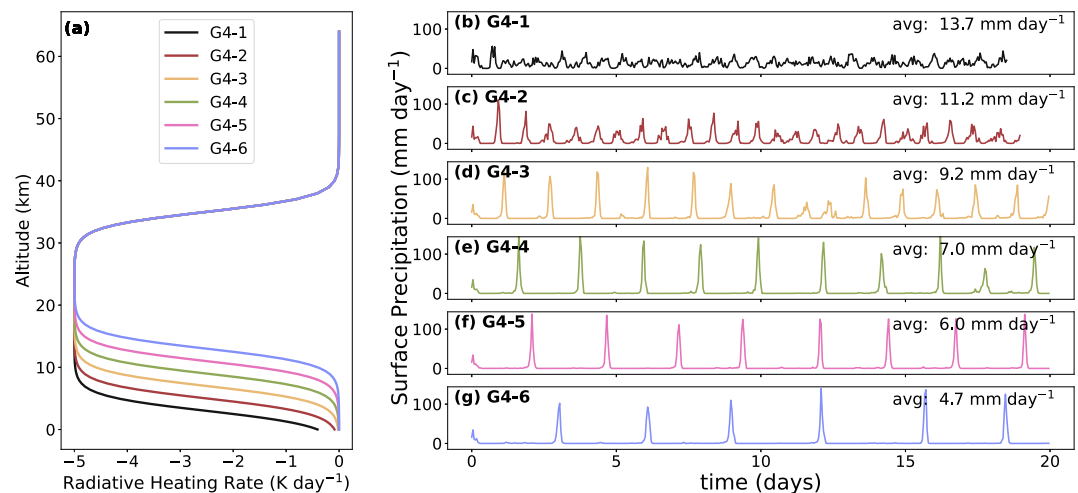
Figure 8. Simulations with fixed lower-tropospheric and upper-tropospheric heating rates but different tops of the lower troposphere (z_0). Panel (a) shows the prescribed radiative heating rate profiles. The lower-tropospheric heating rate is 0 K day^{-1}, and the upper-tropospheric heating rate is -5 K day^{-1}. z_0 in panels (b) to (g) are 3, 5, 7, 9, 11, and 13 km, respectively.

rate, and quasi-steady precipitation with negative lower-tropospheric heating rate. According to these three types, we choose three representative experiments from Section 3.1 to study the mechanism of the episodic deluges. Figure 9 shows the analyses. The left column shows an example of episodic deluges with a lower-tropospheric heating rate of 0.2 K day^{-1} (Figures 9a and 9d). The middle column shows an example of episodic deluges with a negative lower-tropospheric heating rate of -0.2 K day^{-1} (Figures 9b and 9e). The right column shows an example of quasi-steady precipitation with a negative lower-tropospheric heating rate of -0.8 K day^{-1} (Figures 9c and 9f). The upper-tropospheric radiative heating rates are all -1.5 K day^{-1}, and the top of the lower troposphere is 8 km.

First, we try to understand the mechanism through temperature lapse rate, by analyzing potential temperature (θ) and saturated equivalent potential temperature (θ_{se}). Potential temperature (θ) is conserved for dry adiabatic processes. For dry air, $\frac{\partial \theta}{\partial z} \geq 0$ indicates stability, but moist air can be conditionally unstable in this situation (Yau & Rogers, 1996). Saturated equivalent potential temperature (θ_{se}) is conserved for a reversible moist adiabatic process. When $\frac{\partial \theta_{se}}{\partial z} \geq 0$, the temperature lapse rate is smaller than the moist adiabatic lapse rate, and the air is stable (Emanuel, 1994). θ_{se} is a useful measure of the static stability of a saturated atmosphere. When the lower-tropospheric radiative heating rate is positive (Figure 9a), the θ_{se} profile has a strong inversion at ≈ 1 km, but has almost no obvious inversion above 2 km (red line in Figure 9j). The θ_{se} inversion at ≈ 1 km is unlikely to be important for suppressing the convection; Figures 3c and 3d suggest that the lower troposphere reaches up to 10 km (see also Figure 3 in Seeley and Wordsworth (2021)). Moreover, when we remove the heating at 1–2 km in the polar night experiment, episodic deluges still occur (Figure 3). When the lower-tropospheric radiative heating rate is negative (Figures 9b and 9c), the θ_{se} profiles of the -0.2 K day^{-1} case and the -0.8 K day^{-1} case (Figures 9k and 9l) appear broadly similar, but only the -0.2 K day^{-1} case has episodic deluges (Figure 9e). Therefore, for episodic deluges, θ_{se} does not appear to yield insight into the location of the lower troposphere. In what follows, we analyze the experiments through a different angle.

The difference in convective available potential energy (CAPE) and convective inhibition (CIN) at the start and end of the precipitation is large (Figures 9m and 9p), suggesting another possible way to understand the episodic deluges. CAPE is defined as

$$\text{CAPE} = R_d \int_{p(\text{LFC})}^{p(\text{EL})} (T_{ve} - T_{vp})\, d\ln(p), \tag{3}$$

where R_d is the gas constant for dry air, LFC is the level of free convection, EL is the level of neutral buoyancy, T_{ve} is the virtual temperature of the environment, and T_{vp} is the virtual temperature of the rising air parcel (Riemann-Campe et al., 2009; Williams & Renno, 1993). CAPE shows the total energy available for convection (Emanuel, 1994), but large CAPE does not guarantee the occurrence of strong convection. To release CAPE, the air parcel needs to overcome the negative buoyancy from the environment and rise high enough. CIN measures the intensity of the inhibition energy, and is defined as

$$\text{CIN} = R_d \int_{p(\text{SFC})}^{p(\text{LFC})} (T_{ve} - T_{vp})\, d\ln(p), \tag{4}$$

where SFC is the surface. The value of CIN indicates the amount of energy an air parcel needs to overcome to initiate convection (Colby Jr, 1984; Riemann-Campe et al., 2009; Williams & Renno, 1993), and the value of CAPE indicates how strong the convection will be if convection occurs (Emanuel, 1994; Moncrieff & Miller, 1976; Rennó & Ingersoll, 1996). Note that CIN is always negative. The more negative CIN is, the stronger the inhibition is.

Figure 10 shows the time series of CAPE and CIN for the experiments in G1. When the precipitation pattern is episodic, CAPE decreases and CIN gets significantly more negative after the deluge. The strongly negative CIN inhibits convection. During the inhibition period, CAPE increases while CIN weakens as a function of time. When CIN is too weak to inhibit convection, convection starts, and the strong CAPE release causes an intense deluge.
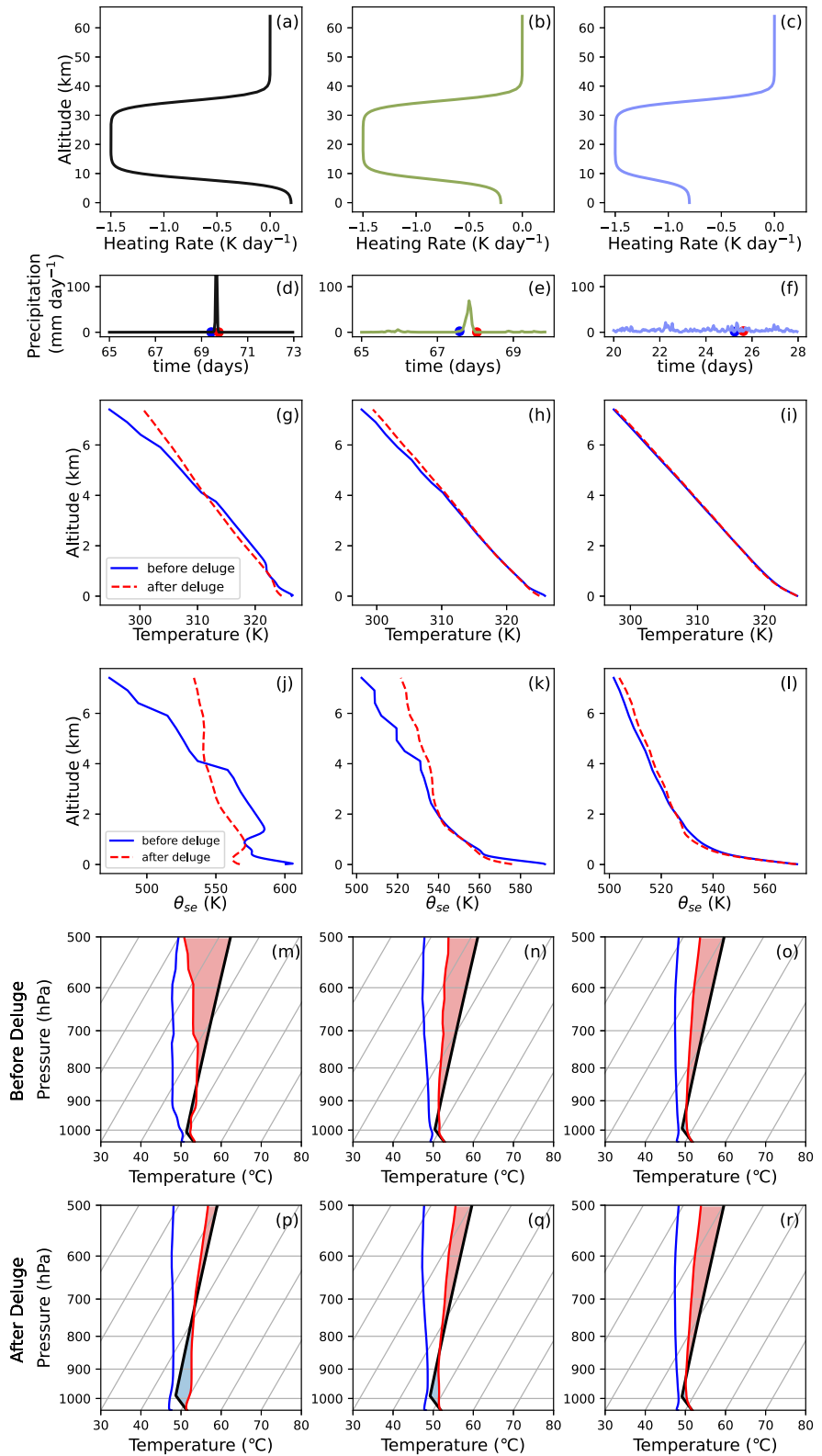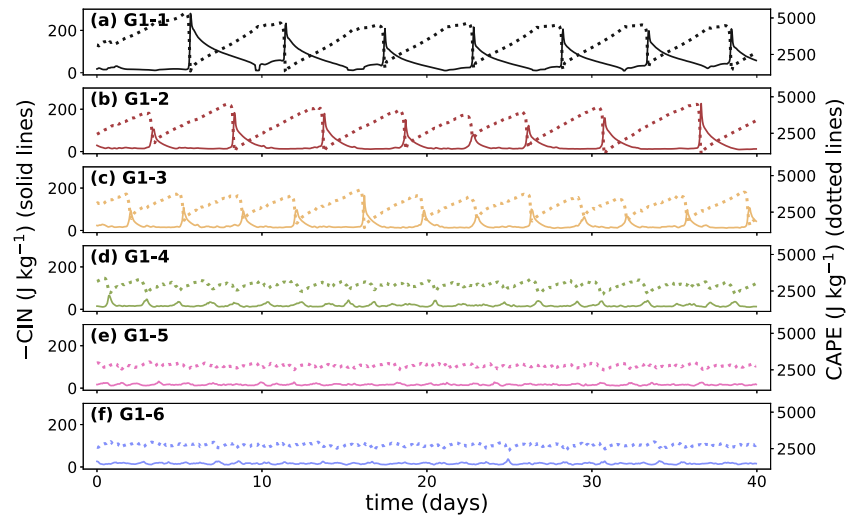
Figure 9.

Figure 10. The time series of convective inhibition (CIN) and convective available potential energy (CAPE) for the experiments in Figure 5. We plot the negative value of CIN for clarity.

Table 1 shows the average and the 2-σ control limits of CIN and CAPE for all the experiments. For the experiments with episodic deluges, the CIN value 2-σ below the mean is less than -50 J kg^{-1}. CAPE does not differ much between episodic or quasi-steady precipitation experiments. The experiments in group G1 show that episodic deluge cases tend to have strong CIN and CAPE. The experiments in group G2 show that large CAPE alone is not enough to trigger episodic deluges. The experiments in group G4 show that when CIN is strong enough, even if CAPE is a bit small, for example, G4-2, episodic deluges still occur. The results are consistent with the common view that CIN indicates the strength of convective inhibition and CAPE indicates how strong the convection is (Colby Jr, 1984; Emanuel, 1994).

In short, the onset of episodic deluges depends on two conditions. First, the lower-tropospheric radiative heating rate should be close to zero (it can be slightly negative or positive) to maintain an inhibition period. Second, the upper-tropospheric cooling rate should be strong enough to increase the temperature lapse rate and trigger strong convection. Therefore, we use the ratio of the lower-tropospheric heating rate to the upper-tropospheric heating rate as an index of the vertical gradient in radiative cooling (Figure 11). We find that the precipitation is episodic when this index is smaller than 0.5, and is non-episodic when this index is larger than 0.5.

Why choose the above index? Because the ratio of the lower-tropospheric heating rate to the upper-tropospheric heating rate is the key factor for creating a large vertical temperature gradient. When the lower-tropospheric heating rate is -0.8 K day^{-1}, a -1.5 K day^{-1} upper-tropospheric heating rate is not strong enough compared with the lower-tropospheric heating rate (Figure 9c). The resulting temperature gradient is too small to trigger strong convection, and the energy release during convection is not large enough to start an inhibition period, so CIN and CAPE do not change much before and after precipitation (Figures 9o and 9r). The differences in the temperature and θ_{se} profiles before and after the precipitation are also small (Figures 9i and 9l). When the lower-tropospheric heating rate is -0.2 K day^{-1}, a -1.5 K day^{-1} upper-tropospheric heating rate is strong enough to cause episodic deluges (Figure 9b). The differences in the temperature and θ_{se} profiles before and after the deluge are obvious (Figures 9h and 9k). The big difference in CIN and CAPE before and after the deluge (Figures 9n and 9q) is necessary to maintain the oscillation of the deluges.

Figure 12 shows a schematic diagram of what happens before and after a deluge. During the inhibition period, CIN is strongly negative, suppressing convection. The strong radiative cooling in the upper troposphere "drags"

Figure 9. The specified radiative heating rate profiles, precipitation time series, air temperature, saturated equivalent potential temperature, and CAPE and CIN before and after a convection event leading to an above-average (strong) precipitation. Panels in the left, middle, and right columns correspond to the experiments in Figures 5b, 5d, and 5f, with lower-tropospheric heating rates of 0.2, -0.2, and, -0.8 K day^{-1}, respectively. In the two bottom rows, the blue, black, and red lines are dew point temperature, parcel temperature, and environmental temperature, respectively. Red and blue shades in panels (m)–(o) show the CAPE and CIN before strong precipitation, and shades in panels (p)–(r) show the CAPE and CIN after strong precipitation.
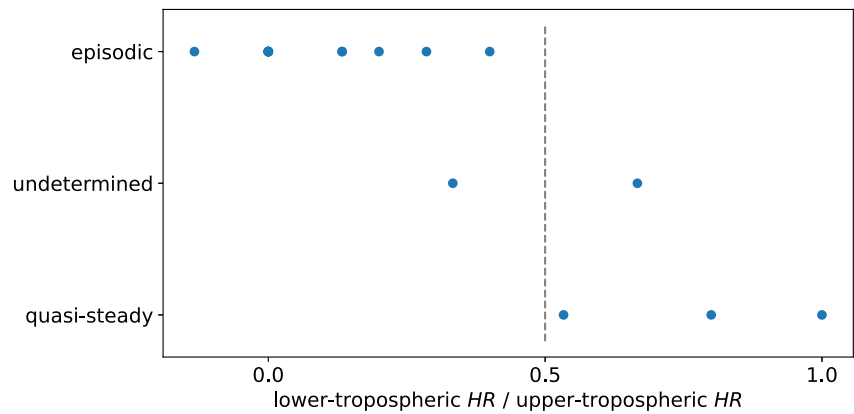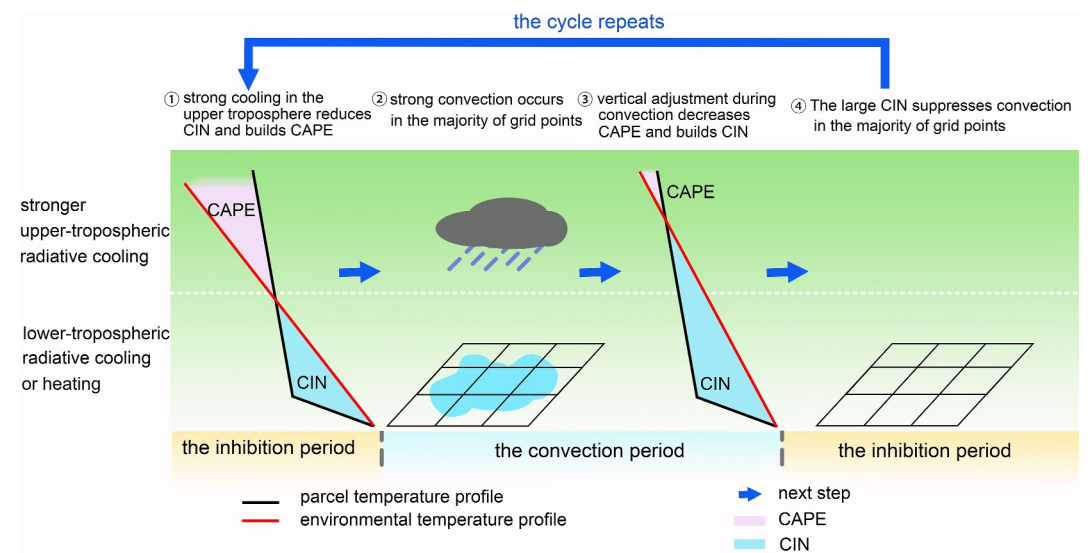
Figure 11. Relative heating rate threshold for episodic deluges. The horizontal axis shows the ratio of the lower-tropospheric radiative heating rate to the upper-tropospheric radiative heating rate (heating rates are positive, cooling rates are negative). Each circle stands for a simulation. Precipitation is episodic when the ratio of lower-tropospheric heating rate to upper-tropospheric heating rate is less than about 0.5.

the temperature profile to a greater lapse rate, and reevaporation in the lower troposphere also helps weaken CIN and build CAPE (step 1). The cooling process triggers strong convection in the majority of grid points (step 2). The energy release during heavy precipitation adjusts the temperature profile to have a much smaller gradient and CIN intensifies (step 3). The majority of grid points do not precipitate under a small vertical temperature gradient and strong CIN, showing an inhibition period (step 4). Then, the cycle repeats again, with strong radiative cooling in the upper troposphere increasing the lapse rate again and triggering the next deluge.

3.5. What Determines the Period of the Episodic Deluges?

The simulations in Sections 3.1–3.3 have different periods of the cycle of episodic deluge. To understand these periods, let's start from the basic temperature equation (Vallis, 2019)

$$\frac{\partial T}{\partial t} = -\left(u\frac{\partial}{\partial x} + v\frac{\partial}{\partial y} + w\frac{\partial}{\partial z}\right)T - \frac{RT}{c_v}\nabla \cdot \vec{v} + \nabla^2(\kappa T) + \frac{J}{c_v}, \tag{5}$$

Figure 12. Schematic diagram of the processes before and after the deluge. Black lines are the parcel temperature profiles, and red lines are environmental temperature profiles. The white dotted lines indicate z_0, the boundary height between the lower and upper troposphere. The blue arrows point to the next step.
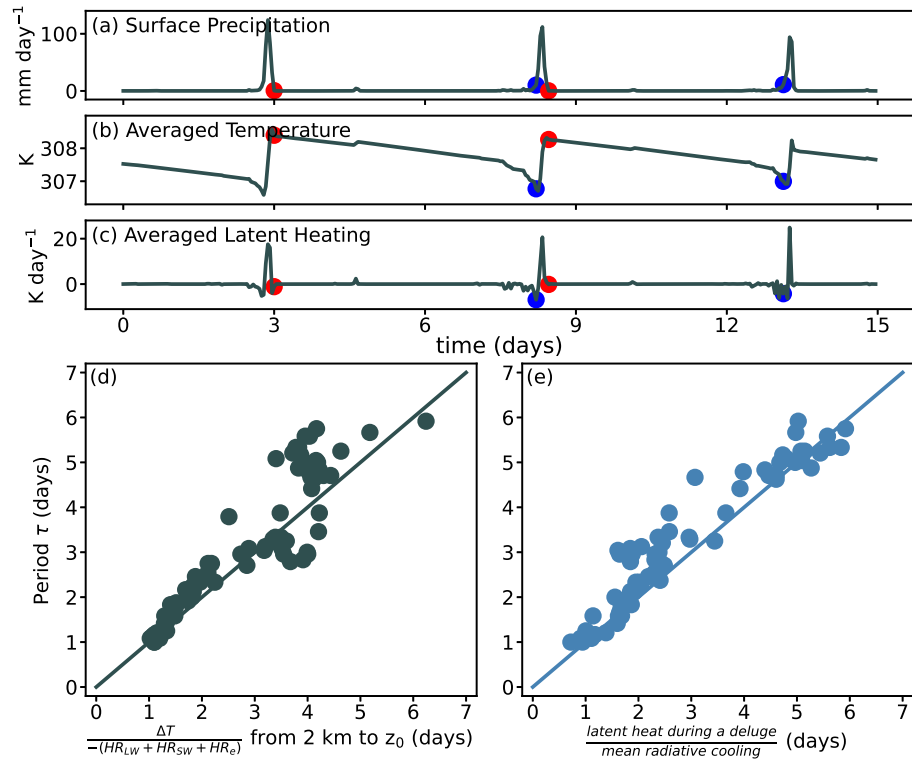
Figure 13. (a–c) Surface precipitation (a) and time series of vertically averaged temperature (b) and latent heating (c) in the lower troposphere. An inhibition period starts from the end of previous precipitation (red dot), and ends at the beginning of the next precipitation (blue dot). (d–e) The model output period Δt compared with the calculated theoretical period using Equation 6 (d), and the ratio of the latent heating during a deluge to the mean tropospheric radiative cooling (e). A 1:1 line is plotted for reference. Note that we remove those episodic deluge experiments with unclear boundary between inhibition periods and convection periods, such as experiments G1-4, G2-4, and G4-2.

where R is the molar gas constant (8.31 J mol^{-1} K^{-1}); c_v is the specific heat capacity under fixed volume (718 J kg^{-1} K^{-1}); κ is the thermal diffusivity representing the effect of thermal diffusion and subgrid mixing; J is the external heating source including longwave cooling, shortwave heating, latent heat release through condensation, and latent cooling by reevaporation. Each experiment in this study is in a small domain and without the Coriolis force, so the horizontal temperature gradient is small, and horizontal advection $\left(u\frac{\partial T}{\partial x} + v\frac{\partial T}{\partial y}\right)$ is negligible. The deluges end rather quickly, so the period of episodic deluges is essentially the time span of the inhibition period. During the inhibition period, the vertical advection $\left(w\frac{\partial T}{\partial z}\right)$ and thermodynamic work $\left(\frac{RT}{c_v}\nabla \cdot \vec{v}\right)$ done by the air parcel in the lower troposphere are also negligible. The influence of temperature diffusion, $\nabla^2(\kappa T)$, is small compared with the timescale of diabatic heating (J). Therefore, diabatic heating alone is the main source of air temperature change. Seeley and Wordsworth (2021) showed that precipitation reevaporation cools down the lower troposphere and breaks the inhibition. Apart from reevaporation cooling, radiative cooling is also a way of diabatic cooling. The period of episodic deluges is determined by how much time radiation and reevaporation cool down the lower troposphere. The equation is given by

$$\Delta t \approx \frac{\Delta T}{-(HR_{LW} + HR_{SW} + HR_e)}, \tag{6}$$

where $-(HR_{LW} + HR_{SW})$ is the radiative cooling rate and $-HR_e$ is the reevaporation cooling rate. All the variables are the time mean and vertically averaged from 2 km to the top of the lower troposphere.

Figure 13d compares the model output period τ with the calculated theoretical period Δt (Equation 6). Each circle stands for a single inhibition period. The inhibition period starts from the end of a deluge when precipitation drops

to the inhibition period level, and ends at the beginning of the next deluge when precipitation starts to increase sharply (Figure 13a). This result supports the idea that radiative cooling and reevaporation cooling control the period of episodic deluges.

The combined effect of radiative cooling and reevaporation cooling can quantitively explain the period differences in Figures 5, 6, and 8. In the experiments G1 with different lower-tropospheric heating rates (Figure 5), the stronger radiative cooling is, the larger the denominator in Equation 6 is, and the quicker the cooling process is. As the lower-tropospheric radiative heating rate decreases, the inhibition period shortens, until finally the inhibition period almost vanishes and the precipitation pattern becomes quasi-steady.

In the G2 group of experiments, we fix the lower-tropospheric radiative heating rate at -0.2 K day^{-1} and change the upper-tropospheric cooling rate (Figure 6). A stronger upper-tropospheric radiative cooling results in more condensation in the upper troposphere, so more precipitation droplets reevaporate in the lower troposphere, and the denominator in Equation 6 increases. The increasing reevaporation cooling leads to shorter period. In the G4 group of experiments with different heights of the lower troposphere top (Figure 8), the lower-tropospheric radiative cooling rate is zero for all the cases, so reevaporation cooling controls the periods. Higher top of the lower troposphere means weaker total radiative cooling, so less precipitation from the upper troposphere enters the lower troposphere and the denominator in Equation 6 decreases, and therefore the period is longer and the inhibition periods are drier.

Apart from calculating the lower-layer cooling, the period of episodic deluges can also be diagnosed through the energy budget. Figure 13e uses the ratio of the latent heating during a deluge to the mean tropospheric radiative cooling as an approximation of the period. This new metric performs well with our simulations, but needs fewer parameters.

4. Summary and Discussion

In this paper, we refine and add detail to the episodic deluge theory developed by Seeley and Wordsworth (2021). We show that episodic deluges can occur during polar night, which indicates that shortwave heating is not a necessary condition for episodic deluges. Moreover, we show that episodic deluges can occur even if the lower-tropospheric radiative heating rate is negative. We perform multiple groups of experiments to show that the vertical gradient of the radiative heating rate profile is an important factor for the onset of episodic deluges. All of our episodic deluge experiments have relatively large convective inhibition (CIN), but we cannot clearly explain how the value of CIN is linked to the inhibition mechanism.

We find three factors that influence the period of episodic deluges: lower-tropospheric radiative heating rate (γ_0), the upper-tropospheric radiative heating rate (γ_1), and the lower-troposphere height (z_0). Generally, a higher z_0, stronger radiative heating in the lower-troposphere, or weaker radiative cooling in the upper troposphere leads to a longer period. We calculate the period of episodic deluge in two ways. The period matches the time for radiation and reevaporation to cool down the lower troposphere, and also matches the ratio of the latent heating during a deluge to the mean tropospheric radiative cooling.

Another interesting factor is that the heating rate in the 325 K case is nearly horizontally uniform in a small domain (Figures 1f and 1g; on the other hand, it is possible that the homogeneity of radiative heating is an artifact of a small domain size). The homogeneity of radiative heating rates may be an important factor for episodic deluges, as it causes a spatial coordination among the grid points, so that heavy precipitation occurs at the same time in the majority, over 65%, of grid points (Figure 3f). The coordinated inhibition–convection–inhibition cycle in the majority of grid points demonstrates an episodic deluge pattern in a macroscopic view. In small domains, if the precipitation behavior among the grid points is not coordinated, convection occurs here and there at different times in different grid points, demonstrating a random, or quasi-steady, precipitation pattern in a macroscopic view (not shown). Consider, for example, the radiative heating rates in the reproduction experiments (Figures 1d–1g). When the surface temperature is 305 K, both lower-tropospheric heating and strong upper-tropospheric cooling exist, but not in the majority of the grid points (Figures 1d and 1e), so the precipitation pattern is quasi-steady. When the surface temperature is 325 K, lower-tropospheric heating and strong upper-tropospheric cooling may not be as strong as in some grid points in the 305 K case during the inhibition period, but they are more wide spread in over 65% of the grid points (Figures 1f and 1g), so the precipitation pattern is episodic. These observations suggest an intimate connection between convective organization in time and space. Muller and

Held (2012) found that for an SST of 300 K self-aggregation still occurred with homogenized shortwave heating, but homogenized longwave cooling prevents self-aggregation regardless of the domain size or resolution. The importance of homogeneous radiative heating rates for episodic deluge in hothouse climates (>320 K) needs further study. Could episodic deluges still exist with inhomogeneous radiative heating? We plan to modify the horizontal distribution of the radiative heating rate and examine how precipitation changes in future studies.

Apart from this work, two recent studies, Dagan et al. (2023) and Spaulding-Astudillo and Mitchell (2023), also focus on the temporal variability of precipitation under hothouse climates. Dagan et al. (2023) conducted a simulation with domain size up to 6,144 km × 384 km, with mean SST of 325 K, and with SST gradient and interactive radiation. On the domain-mean scale, the precipitation demonstrates a pattern of short deluges followed by long and dry periods, but is less synchronized. Spaulding-Astudillo and Mitchell (2023) show that episodic deluges exist even in a 1D single-column radiative-convective model although the period of the episodic deluges is several years, much longer than the several-day period in 3D radiative-convective model. They also show that lower-tropospheric radiative heating is not necessary for the onset of the episodic deluges.

Here we study episodic deluges in a small domain, and do not include rotation and the Coriolis force, thus many weather phenomena, such as midlatitude cyclones caused by baroclinic instability, cannot be considered. In large-scale modeling, with the influence of Hadley and Walker cells, cyclones and anti-cyclones, large-scale horizontal advection is no longer negligible, and more factors, such as dynamic lifting, can possibly break inhibition. Can episodic deluges exist in global-scale simulations? How do episodic deluges interact with global circulation and climate? These questions are worthy of further study.

## Appendix A: Experiment Results With Discontinuous Heating Rate Profiles

Figures A1–A4 show the experiment results with heating rate profiles that are discontinuous at z_0 and at 35 km.
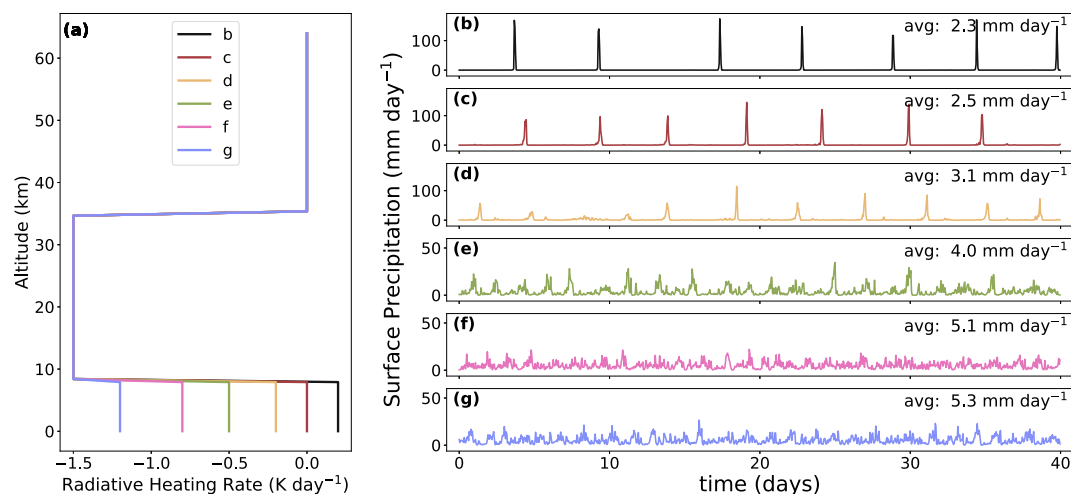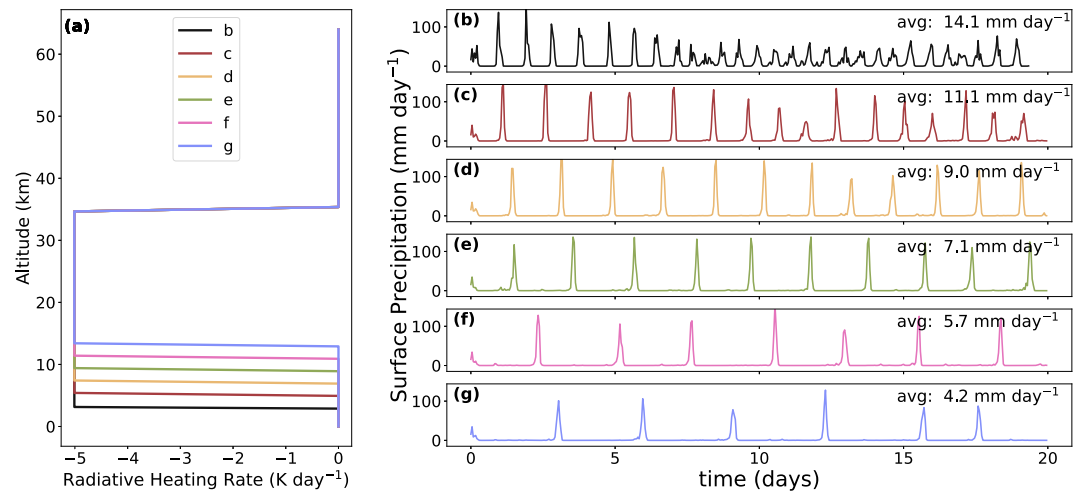

Figure A1. Same as the control group experiments of Figure 5, but the heating rate is discontinuous at the top of the lower troposphere (z_0) and at the stratosphere (35 km). Panel (a) shows the prescribed radiative heating rate profiles. The upper-tropospheric heating rate is -1.5 K day^{-1}. The lower-tropospheric heating rates in panels (b) to (g) are 0.2, 0, -0.2, -0.5, -0.8, and -1.2 K day^{-1}, respectively. The top of the lower troposphere is 8 km.
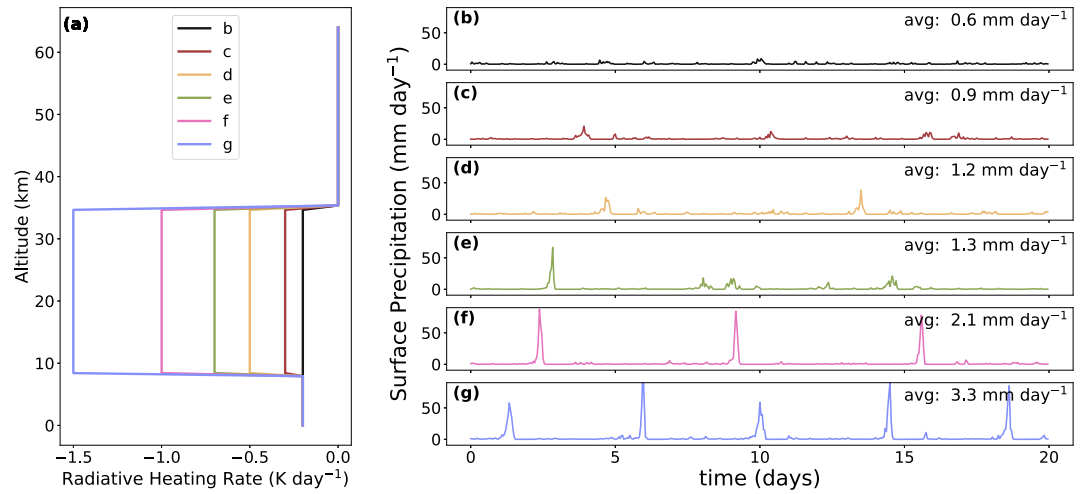
Figure A2. Same as the control group experiments of Figure 6, but the heating rate is discontinuous at z_0 and at 35 km. Panel (a) shows the prescribed radiative heating rate profiles. The lower-tropospheric heating rate is -0.2 K day^{-1}. The upper-tropospheric heating rates in panels (b) to (g) are -0.2, -0.3, -0.5, -0.7, -1.0, and -1.5 K day^{-1}, respectively. The top of the lower troposphere is 8 km.
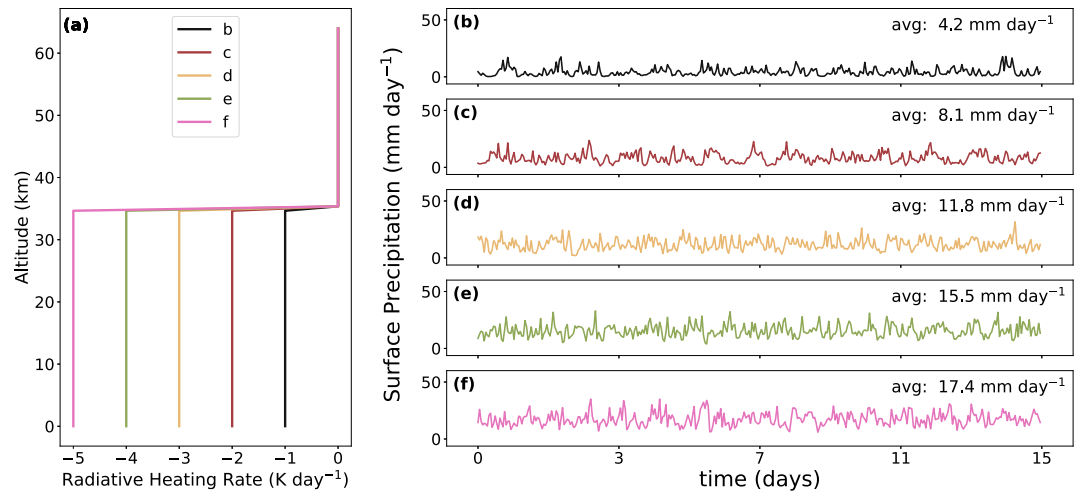
Figure A3. Same as the control group experiments of Figure 7, but the heating rate is discontinuous at 35 km. Panel (a) shows the prescribed radiative heating rate profiles. The lower-tropospheric heating rates and the upper-tropospheric heating rates in panels (b) to (f) are -1, -2, -3, -4, and -5 K day^{-1}, respectively.

Figure A4. Same as the control group experiments of Figure 8, but the heating rate is discontinuous at z_0 and at 35 km. Panel (a) shows the prescribed radiative heating rate profiles. The lower-tropospheric heating rate is 0 K day^{-1}, and the upper-tropospheric heating rate is -5 K day^{-1}. The top of the lower troposphere in panels (b) to (g) is 3, 5, 7, 9, 11, and 13 km, respectively.

Data Availability Statement

The cloud-resolving model SAM is publicly available at M. Khairoutdinov (2004). The data in this study is publicly available at Song et al. (2023).

References

Bryan, G. H., & Fritsch, J. M. (2002). A benchmark simulation for moist nonhydrostatic numerical models. *Monthly Weather Review*, *130*(12), 2917–2928. https://doi.org/10.1175/1520-0493(2002)130<2917:absfmn>2.0.co;2

Charnay, B., Hir, G. L., Fluteau, F., Forget, F., & Catling, D. C. (2017). A warm or a cold early Earth? New insights from a 3-D climate-carbon model. *Earth and Planetary Science Letters*, *474*, 97–109. https://doi.org/10.1016/j.epsl.2017.06.029

Colby Jr, F. P. (1984). Convective inhibition as a predictor of convection during AVE-SESAME II. *Monthly Weather Review*, *112*(11), 2239–2252. https://doi.org/10.1175/1520-0493(1984)112<2239:CIAAPO>2.0.CO;2

Collins, W. D., Rasch, P. J., Boville, B. A., Hack, J. J., McCaa, J. R., Williamson, D. L., et al. (2006). The formulation and atmospheric simulation of the Community Atmosphere Model version 3 (CAM3). *Journal of Climate*, *19*(11), 2144–2161. https://doi.org/10.1175/jcli3760.1

Dagan, G., Seeley, J. T., & Steiger, N. (2023). Convection and convective-organization in hothouse climates. *Journal of Advances in Modeling Earth Systems*, *15*(11), e2023MS003765. https://doi.org/10.1029/2023MS003765

Emanuel, K. (1994). *Atmospheric convection*. Oxford University PressNew. https://doi.org/10.1093/oso/9780195066302.001.0001

Gini, C. (1997). Concentration and dependency ratios. *Rivista di Politica Economica*, *87*, 769–792.

Goldblatt, C., Robinson, T. D., Zahnle, K. J., & Crisp, D. (2013). Low simulated radiation limit for runaway greenhouse climates. *Nature Geoscience*, *6*(8), 661–667. https://doi.org/10.1038/ngeo1892

Higgins, J. A., & Schrag, D. P. (2003). Aftermath of a snowball Earth. *Geochemistry, Geophysics, Geosystems*, *4*(3), 1028. https://doi.org/10.1029/2002gc000403

Hir, G. L., Donnadieu, Y., Goddéris, Y., Pierrehumbert, R. T., Halverson, G. P., Macouin, M., et al. (2009). The snowball Earth aftermath: Exploring the limits of continental weathering processes. *Earth and Planetary Science Letters*, *277*(3–4), 453–463. https://doi.org/10.1016/j.epsl.2008.11.010

Hoffman, P. F., Abbot, D. S., Ashkenazy, Y., Benn, D. I., Brocks, J. J., Cohen, P. A., et al. (2017). Snowball Earth climate dynamics and Cryogenian geology-geobiology. *Science Advances*, *3*(11), e1600983. https://doi.org/10.1126/sciadv.1600983

Ingersoll, A. P. (1969). The runaway greenhouse: A history of water on Venus. *Journal of the Atmospheric Sciences*, *26*(6), 1191–1198. https://doi.org/10.1175/1520-0469(1969)026⟨1191:trgaho⟩2.0.co;2

Kasting, J. F., Pollack, J. B., & Ackerman, T. P. (1984). Response of Earth's atmosphere to increases in solar flux and implications for loss of water from Venus. *Icarus*, *57*(3), 335–355. https://doi.org/10.1016/0019-1035(84)90122-2

Khairoutdinov, M. (2004). Sam model code [Software]. *MSRC*. Retrieved from http://rossby.msrc.sunysb.edu/SAM.html

Khairoutdinov, M. F., & Emanuel, K. (2018). Intraseasonal variability in a cloud-permitting near-global equatorial aquaplanet model. *Journal of the Atmospheric Sciences*, *75*(12), 4337–4355. https://doi.org/10.1175/jas-d-18-0152.1

Khairoutdinov, M. F., & Randall, D. A. (2003). Cloud resolving modeling of the ARM summer 1997 IOP: Model formulation, results, uncertainties, and sensitivities. *Journal of the Atmospheric Sciences*, *60*(4), 607–625. https://doi.org/10.1175/1520-0469(2003)060⟨0607:crmota⟩2.0.co;2

Kidder, D. L., & Worsley, T. R. (2012). A human-induced hothouse climate? *Geological Society of America Today*, 4–11. https://doi.org/10.1130/g131a.1

Koll, D. D. B., & Cronin, T. W. (2018). Earth's outgoing longwave radiation linear due to H₂O greenhouse effect. *Proceedings of the National Academy of Sciences of the United States of America*, *115*(41), 10293–10298. https://doi.org/10.1073/pnas.1809868115

Leconte, J., Forget, F., Charnay, B., Wordsworth, R., & Pottier, A. (2013). Increased insolation threshold for runaway greenhouse processes on Earth-like planets. *Nature*, *504*(7479), 268–271. https://doi.org/10.1038/nature12827

Mlawer, E. J., Taubman, S. J., Brown, P. D., Iacono, M. J., & Clough, S. A. (1997). Radiative transfer for inhomogeneous atmospheres: RRTM, a validated correlated-k model for the longwave. *Journal of Geophysical Research*, *102*(D14), 16663–16682. https://doi.org/10.1029/97jd00237

Moncrieff, M. W., & Miller, M. J. (1976). The dynamics and simulation of tropical cumulonimbus and squall lines. *Quarterly Journal of the Royal Meteorological Society*, *102*(432), 373–394. https://doi.org/10.1002/qj.49710243208

Muller, C. J., & Held, I. M. (2012). Detailed investigation of the self-aggregation of convection in cloud-resolving simulations. *Journal of the Atmospheric Sciences*, *69*(8), 2551–2565. https://doi.org/10.1175/jas-d-11-0257.1

Pierrehumbert, R., Abbot, D., Voigt, A., & Koll, D. (2011). Climate of the Neoproterozoic. *Annual Review of Earth and Planetary Sciences*, *39*(1), 417–460. https://doi.org/10.1146/annurev-earth-040809-152447

Popp, M., Schmidt, H., & Marotzke, J. (2016). Transition to a moist greenhouse with CO_2 and solar forcing. *Nature Communications*, *7*(1). https://doi.org/10.1038/ncomms10627

Ramirez, R. M., Kopparapu, R. K., Lindner, V., & Kasting, J. F. (2014). Can increased atmospheric CO_2 levels trigger a runaway greenhouse? *Astrobiology*, *14*(8), 714–731. https://doi.org/10.1089/ast.2014.1153

Rennó, N. O., & Ingersoll, A. P. (1996). Natural convection as a heat engine: A theory for CAPE. *Journal of the Atmospheric Sciences*, *53*(4), 572–585. https://doi.org/10.1175/1520-0469(1996)053⟨0572:NCAAHE⟩2.0.CO;2

Riemann-Campe, K., Fraedrich, K., & Lunkeit, F. (2009). Global climatology of convective available potential energy (CAPE) and convective inhibition (CIN) in ERA-40 reanalysis. *Atmospheric Research*, *93*(1–3), 534–545. https://doi.org/10.1016/j.atmosres.2008.09.037

Romps, D. M. (2008). The dry-entropy budget of a moist atmosphere. *Journal of the Atmospheric Sciences*, *65*(12), 3779–3799. https://doi.org/10.1175/2008jas2679.1

Seeley, J. T., & Jeevanjee, N. (2021). H_2O windows and CO_2 radiator fins: A clear-sky explanation for the peak in equilibrium climate sensitivity. *Geophysical Research Letters*, *48*(4), e2020GL089609. https://doi.org/10.1002/essoar.10503539.1

Seeley, J. T., & Wordsworth, R. D. (2021). Episodic deluges in simulated hothouse climates. *Nature*, *599*(7883), 74–79. https://doi.org/10.1038/s41586-021-03919-z

Sleep, N. H. (2010). The Hadean-Archaean environment. *Cold Spring Harbor Perspectives in Biology*, *2*(6), a002527. https://doi.org/10.1101/cshperspect.a002527

Song, X., Abbot, D. S., & Yang, J. (2023). Data for the paper: Critical role of radiative cooling vertical contrast in triggering episodic deluges in small-domain hothouse climates [Dataset]. *Zenodo*. https://doi.org/10.5281/zenodo.8103889

Spaulding-Astudillo, F. E., & Mitchell, J. L. (2023). The emergence of relaxation-oscillator convection on earth and titan. arXiv preprint arXiv:2306.03219.

Steffen, W., Rockström, J., Richardson, K., Lenton, T. M., Folke, C., Liverman, D., et al. (2018). Trajectories of the Earth system in the Anthropocene. *Proceedings of the National Academy of Sciences*, *115*(33), 8252–8259. https://doi.org/10.1073/pnas.1810141115

Vallis, G. (2019). *Essentials of atmospheric and oceanic dynamics*. Cambridge University Press.

Williams, E., & Renno, N. (1993). An analysis of the conditional instability of the tropical atmosphere. *Monthly Weather Review*, *121*(1), 21–36. https://doi.org/10.1175/1520-0493(1993)121⟨0021:aaotci⟩2.0.co;2

Wolf, E., Haqq-Misra, J., & Toon, O. (2018). Evaluating climate sensitivity to CO_2 across Earth's history. *Journal of Geophysical Research: Atmospheres*, *123*(21), 11–861. https://doi.org/10.1029/2018jd029262

Wolf, E., & Toon, O. B. (2015). The evolution of habitable climates under the brightening sun. *Journal of Geophysical Research: Atmospheres*, *120*(12), 5775–5794. https://doi.org/10.1002/2015jd023302

Wordsworth, R., & Pierrehumbert, R. (2013). Water loss from terrestrial planets with CO_2-rich atmospheres. *The Astrophysical Journal*, *778*(2), 154. https://doi.org/10.1088/0004-637x/778/2/154

Yang, J., Jansen, M. F., Macdonald, F. A., & Abbot, D. S. (2017). Persistence of a freshwater surface ocean after a snowball Earth. *Geology*, *45*(7), 615–618. https://doi.org/10.1130/g38920.1

Yang, J., Leconte, J., Wolf, E. T., Goldblatt, C., Feldl, N., Merlis, T., et al. (2016). Differences in water vapor radiative transfer among 1D models can significantly affect the inner edge of the habitable zone. *The Astrophysical Journal*, *826*(2), 222. https://doi.org/10.3847/0004-637X/826/2/222

Yau, M. K., & Rogers, R. R. (1996). *A short course in cloud physics*. Elsevier.